PHYSICAL REVIEW B **85**, 245304 (2012)

Nanosecond laser-induced selective removal of the active layer of CuInGaSe$_2$ solar cells by stress-assisted ablation

András Buzás[1,*] and Zsolt Geretovszky[2]

[1] *Institute of Physics, Biological Research Center, Hungarian Academy of Sciences, H-6701 Szeged, P.O. Box 521, Hungary*

[2] *Department of Optics and Quantum Electronics, University of Szeged, Dóm tér 9, H-6720 Szeged, Hungary*

(Received 20 December 2011; published 7 June 2012)

We demonstrate that laser pulses of nanosecond duration ($\lambda = 1064$ nm, $\tau = 25$ ns, PRR $= 5$ kHz) are capable of the clean removal of the CuInGaSe$_2$ (CIGS) and ZnO:Al layers in the layer structure of chalcogenide-based solar cells, leaving the underlying Mo layer undamaged and producing excellent crater morphology. Our results prove that the material removal process is governed by the thermomechanical stress developing in the CIGS layer due to rapid laser heating. In the mechanical ablation of the active layer, three phenomena play a crucial role, namely, delamination, buckling, and fracture. Morphological and compositional analysis of the laser-processed areas is used to identify the experimental parameters where clean mechanical ablation can be achieved. Numerical calculations, performed in the COMSOL software environment, are also presented to complement the experimental tendencies and verify the proposed model. Our calculation proves the development of a stress distribution that drives the delamination of the CIGS and Mo layers. As the delamination front proceeds radially outward, the separation of the layers ceases in the colder outer regions according to the Griffith's criterion and defines the size of the craters produced afterwards. The free-standing chalcogenide layer continues to deform, and buckling results in a growing tensile stress at the perimeter of the delaminated area, where ultimately fracture will finalize the removal process and facilitate the clean ablation of the laser-irradiated area.

DOI: 10.1103/PhysRevB.85.245304 PACS number(s): 81.40.Gh, 68.60.Dv, 79.20.Eb, 68.60.Bs

I. INTRODUCTION

Removal of a coating from the surface of a substrate or an underlying layer stack has many far reaching applications. Some of these applications, such as paint removal or computer-to-press imaging,[1] are more forgiving to the quality of the processed area, while others such as circuit patterning, mask manufacturing, organic electronics (OLED fabrication),[2] or laser scribing of solar panels are more stringent and can not be satisfied by the typical, thermally driven ablation process. Fortunately, ablation is known to occur by a variety of mechanisms, among which the stress-assisted route has several appealing features, such as complete removal of a single or even multiple layers, no surface contamination by debris redeposition, and preserving the performance of any underlying functional layers. As a consequence, laser processing is gradually emerging as a key enabling technology of photovoltaics in general, and of chalcogenide active layer patterning in particular.

Thin-film solar cells having CuInGaSe$_2$ (CIGS) as their active layer are among the most promising due to their high cell efficiency [approaching 20.5% (Ref. 3)] and low fabrication cost. The typical substrate-type CIGS solar cell has the following layer structure: glass/Mo/CIGS/CdS/ZnO:Al, where the glass is used as a support and the ZnO:Al film is the so-called window layer. During the fabrication of a solar module, an array of cells is formed on the substrate. In order to achieve the desired interconnection schemes,[4,5] the layers must be patterned, typically after their deposition steps. The first scribe is an insulating cut, performed on the back contact Mo layer (denoted as P1). The next processing step after the deposition of the absorber CIGS and buffer CdS layers is to form a conducting scribe (P2). Finally, the front contact ZnO:Al window layer must also be patterned (P3) to insulate adjacent cells. The role of the P1 and P3 scribes is to insulate neighboring cells, while that of P2 is to facilitate the connection of front and back contact layers of neighboring cells in series. The efficiency of the so-formed module depends not only on the cell efficiency, but also on the quality of the scribes. Two major losses originate from the patterned area. The first is that the patterned area does not take part in energy conversion, clearly explaining why this area is called the dead zone. The other source of loss is that scribing may result in a shunt and resistance increase at the insulation and conducting scribes, respectively.

It has been proposed that laser processing would be the optimum choice to realize patterning due to its high accuracy and high processing speed coupled with a moderate investment cost.[6] Compaan *et al.* were the first to investigate the pros and cons of laser scribing of CIGS-based solar cell.[6] Nanosecond laser scribing the P2 line in a flexible solar cell was reported by Kessler *et al.*[4] where the removal of the CIGS layer was incomplete, but the remnants of the layer were converted to a conductor. However, they found that this molten CIGS residue increases the resistivity at the ZnO:Al/Mo interface and hence decreases module efficiency.[5] An alternative route for realizing the P2 scribe is the microwelding process where very high laser fluences ($\approx$50 J cm^{-2}) are used to metallize the CIGS layer and form a conduction channel between the Mo and ZnO:Al layers.[7,8] It was also demonstrated for the P2 and P3 laser scribes that the use of picosecond and femtosecond lasers[9–12] results in good channel characteristics. Murrison and co-workers reported the use of a nanosecond laser for performing the P2 and P3 scribes and claim that their appealing scribe characteristics are due to the low absorption of the CIGS, which results in the intensive evaporation at the CIGS/Mo interface.[13]

During laser ablation, many mechanisms are known that may lead to material removal in a multilayer structure, such as evaporation or thermomechanical stress-driven fracture, etc.[14,15] The principal mechanism of the process is jointly determined by the properties of the laser pulse (e.g., pulse duration, wavelength, energy, ...) and the materials' properties of the layer structure (mainly the optical and thermophysical properties of the layers). Hence, due to the different mechanisms, laser ablation may cause a diverse morphology, and chemical and structural phase transitions in and around the laser-processed zone.

When evaporation dominates the removal process, material mainly leaves the substrate in vapor form, while occasionally, due to recoil pressure, the vapor is accompanied by ejected droplets. The strong heating of the material results in a significant heat-affected zone around the processed area, and molten debris remains around the ablation crater.[15] In most situations, chemical and structural phase transitions, such as those mentioned above for the metallization of the CIGS layer via laser melting, may further complicate the overall picture.

Thermomechanical ablation is also common during laser processing of both thin films and multilayer structures. Here, material removal is dominantly driven by stresses building up within a layer or at the interface of different materials. Mechanical stress may also arise via vapor pillow formation at the interfaces.[13,14] During mechanical ablation, material removal takes place (mainly) in the solid phase so the morphology of the processed area is very different from that of an evaporated one.

In this paper, we report our results on laser scribing of the CIGS and ZnO:Al layers in a CIGS solar cell structure. We found that at a given parameter domain, mechanical ablation takes place and results in excellent crater morphology. After describing our experimental observations, we propose a model to describe the mechanical ablation process which is governed by the thermomechanical stress. To verify our mechanical ablation, model numerical calculations were performed using the COMSOL software during which the laser-induced temperature and stress fields in the solar cell structure were modeled as a function of elapsed time.

II. EXPERIMENT

For the experiments, a diode-pumped Nd:YAG laser (Spectra Physics, laser head VHP80-106Q, power supply J20I-8S40-16NSI) was used, operating at the fundamental 1064-nm wavelength, 5-kHz pulse repetition rate, pulse duration of 25 ns [full width at half maximum (FWHM)], and at a maximum average power of $P_{\max} = 400$ mW. The intensity distribution of the laser beam was measured to be a Gaussian.

The laser beam was passed through a polarization-based attenuator system and focused to the sample by a lens. In order to keep the spatial characteristics of beam constant during setting the process power, the laser was always run at 350 mW and the power impinging on the surface of the samples was set by the combination of a voltage-driven retarder and a polarizing cube. The focusing lens is made of BK7 glass, has 10.2 cm focal length at 1064 nm, and is illuminated in its central 6.6-mm-diameter area.

We performed our experiments on substrate-type solar cells grown on glass substrates (Energy Photovoltaics, Inc). The thickness of the individual layers was measured to be 700 nm, 2 μm, 50 nm, and 400 nm for the Mo, CIGS, CdS, and ZnO:Al layers, respectively. In all but one case, the structure was illuminated from above, i.e., the laser beam hit the ZnO:Al layer first. Our experiments were carried out on the entire layer structure, and certain experiments were also repeated on partial solar cell structures where the topmost ZnO:Al layer was chemically removed.

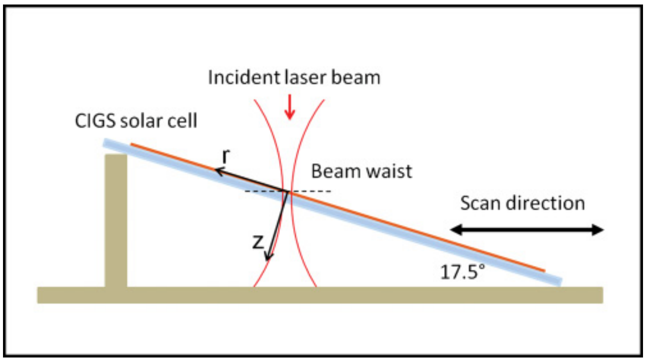

FIG. 1. (Color online) Process geometry.

Figure 1 schematically shows our process geometry. The laser beam was impinging on the sample surface at a 17.5° angle of incidence. With respect to the static laser beam, the sample was scanned perpendicular to the edge of the wedge formed by the sample and its holder. Due to the tilting of the sample with respect to the sample holder, consecutive laser pulses hit the surface at slightly different working distances and, accordingly, the size of the beam at the sample surface was changed pulse by pulse. The working distance was adjusted so that within each scan, the sample surface intersected the laser beam above, at, and below the beam waist. Since the morphology of the laser-processed areas obtained at identical distances below and above the beam waist was practically the same, only those craters were evaluated during the systematic study of the multilayer structure, which were obtained when the beam waist was above the sample surface. It was also ensured that under the conditions used, the laser-matter interaction was independent for consecutive laser shots, i.e., the ablated craters were sufficiently far from each other.

The radius of the laser beam (defined at $1/e^2$ of the peak intensity) was derived following the procedure of Liu[16] by measuring how the ablation crater size depends on laser fluence. For these experiments, craters were laser ablated in a 100-nm-thick Mo layer supported on a glass sample. Figure 2 depicts how the beam radius varies along the optical axis of the lens in the vicinity of the beam waist. The continuous curve shows the calculated values which were determined using the diameter of the laser beam at the position of the focusing lens (measured to be $d = 6.6$ mm at $1/e^2$ of the peak intensity) and the focal length of the lens at 1064 nm wavelength ($f = 10.2/\mathrm{cm}$), while the data set plotted with solid symbols shows the measured beam radii obtained on the Mo layer, wherever the fluence of the laser pulses was sufficient to ablate it. Figure 2 proves that the measured and calculated radii are in good agreement. This agreement also clarifies why we used the calculated beam size values during the course of this study since calculation allows for providing the size of the beam at every working distance, i.e., even at

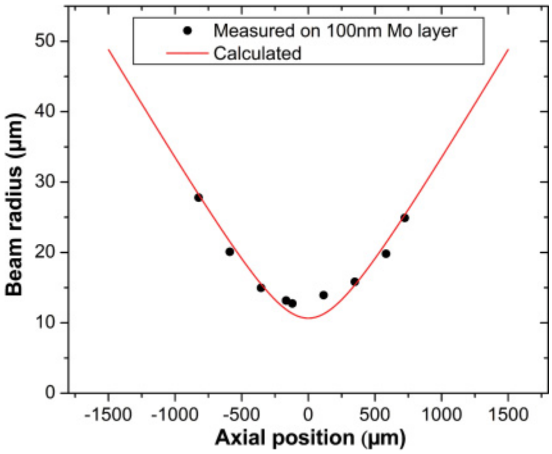

FIG. 2. (Color online) Measured (solid symbols) and calculated (continuous curve) beam radii at different axial positions (corresponding to different working distances).

those positions where the extrapolation of the experimentally obtained radius would be the sole alternative.

Laser-processed areas were routinely characterized by an optical (Nikon Optiphot 100S) and a scanning electron microscope (SEM, model: Hitachi S-4700 FE-SEM). Elemental composition was measured by energy-dispersive x-ray spectrometry (EDS, model: Röntec XFlash QX2) and analyzed using the Quantax microanalysis system. Surface topography was gained from profilometric traces (Dektak 8 surface profiler).

III. DESCRIPTION OF THE MODEL

During computer simulation, the temperature and stress fields were calculated in a multilayer structure identical to that of the samples used for the experiments. In the calculations, the laser-irradiated area was taken to be circular instead of the slightly elliptic one used for the experiments. Neglecting the sample tilt caused only a minor difference since the elliptical irradiated areas were characterized by an aspect ratio of 1.06, i.e., the diameter of the laser beam along the scanning direction was only about 6% larger than in the perpendicular direction. The axes of the cylindrical coordinate system used are indicated in Fig. 1. The zero of the axial coordinate z is located at the air/ZnO interface.

The material properties used are tabulated in Table I. Wherever it was possible, we used temperature-dependent materials properties, however, where such data were unavailable or unreliable, we used and provide data at standard conditions (room temperature, atmospheric pressure) instead. From Table I it is obvious that the Mo, ZnO layers and the glass substrate are well described, but the properties of the active CIGS layer are much unknown. We could not find temperature-dependent data for CIGS and some data (e.g., its Poisson ratio, boiling point, and the enthalpies of melting and boiling) are missing altogether. While the former was handled by performing calculations at several different Poisson numbers between 0.1 and 0.4, in the latter case we had no choice but to avoid those conditions under which melting and boiling of the CIGS layer would occur. In these cases, special emphasis was paid to estimate the effect of these parameters on the calculated result, as will be shown in the following chapters. Due to the lack of information on the relevant materials' properties modeling the inelastic behavior of the sample was not possible, either.

Finally, we note that CdS and CIGS exhibit very similar thermal and mechanical behavior.[6,21] Their relevant thermophysical and mechanical properties differ less than 60%, except one case: CdS is approximately a five times better thermal conductor than CIGS. However, CIGS is 40 times thicker than the CdS layer and hence will dominate the thermal response of this bilayer. Therefore, in our model calculations, the two semiconducting layers were treated as one, and described by the relevant properties of the CIGS layer.

A. Absorption

The laser pulse was modeled as one having Gaussian temporal and spatial distributions. Mathematically, it is defined as

$$\Upsilon(r,t) = I_0 \exp\left(-\frac{2r^2}{w^2}\right)\exp\left(-\frac{4\ln(2)(t-t_p)^2}{t_p^2}\right), \quad (1)$$

where

$$I_0 = 2\sqrt{\frac{\ln(2)}{\pi}}F, \quad (2a)$$

$$F = \frac{2E_{\mathrm{abs}}}{w^2\pi} \quad (2b)$$

are the peak intensity and peak fluence in the center of the laser irradiated area, respectively. In Eqs. (1) and (2), $E_{\mathrm{abs}} = E(1-R)$ denotes the absorbed pulse energy, w is the radius of the laser beam on the sample surface, t_p is the pulse duration at FWHM, and $R = 0.11$ is the net reflectivity of the air/ZnO and ZnO/CIGS interfaces, calculated assuming incoherent superposition. Since the absorption of the ZnO layer is very low, it was neglected in the model. The absorption of the laser beam in the CIGS was described by the Beer-Lambert law so that the laser intensity absorbed within the depth range of 0–z (i.e., in the uppermost part of the CIGS layer) at any radial distance r is given by

$$I(r,z,t) = \begin{cases} 0 \leqslant z \leqslant d_{\mathrm{ZnO}}, & 0 \\ d_{\mathrm{ZnO}} < z \leqslant d_{\mathrm{ZnO}} + d_{\mathrm{CIGS}}, & \Upsilon(r,t)\left(1-e^{-\alpha_{\mathrm{CIGS}}(z-d_{\mathrm{ZnO}})}\right) \\ d_{\mathrm{ZnO}} + d_{\mathrm{CIGS}} < z, & \Upsilon(r,t) \end{cases} \quad (3)$$

TABLE I. Thermophysical properties of the layers. NA stands for Not applicable.

Name	Symbol	Glass[a]	Mo[b]	CIGS[c,d]	ZnO[e]
Melting point (K)	T_m	995	2887	1600	2247
Boiling point (K)	T_b	NA	5442	NA	2310
Enthalpy of melting (kJ kg^{-1})	H_m	NA	290	NA	970
Enthalpy of vaporization (kJ kg^{-1})	H_v	NA	6150	NA	7660
Density (kg m^{-3})	ρ	2500	300–2900 K: $10303–0.2416\,T$	5770	5680
Thermal conductivity (W m^{-1} K^{-1})	k	1	300–2600 K: $152.78–5.0884T$ $+9.6754\times10^{-6}T^2$	3.7	293–412 K: $255.4887–1.665\,393T+0.006\,492\,632T^2$ $-1.361\,659\times10^{-5}T^3+1.102\,392\times10^{-8}T^4$ 412–1073 K: $277.1409–1.140\,114T+0.001\,840\,955T^2$ $-1.338\,889\times10^{-6}T^3+3.666\,218\times10^{-10}T^4$ 1073 K and above: 5.28
Specific heat capacity (J kg^{-1} K^{-1})	c_p	720	300–2600 K: $205.37+0.15586T$ $-8.9568\times10^{-5}T^2$ $+2.721\times10^{-8}T^3$	300	293–693 K: $41.57\,877+3.00\,915T–0.006\,803\,469T^2$ $+7.342\,711\times10^{-6}T^3–3.029\,347\times10^{-9}T^4$ 693–2000 K: $522.6381+0.126\,7524T–1.058\,082\times10^{-5}T^2$ 2000 K and above: 734
Young modulus (GPa)	E	70	300–2900 K: $338.93–3.143\times10^{-2}T$ $-8.2007\times10^{-6}T^2$	75	112
Poisson number	ν	0.2	0.33	0.4[f]	0.3
Thermal expansion (10^{-6} K^{-1})	β	9	300–2900 K: $4.9904+1.1837\times10^{-4}T$ $+3.5877\times10^{-7}T^2$	10	243–2023 K: $2.552\,808+6.581\,276\times10^{-3}T$ $-3.615\,381\times10^{-6}T^2+8.13\,841\times10^{-10}T^3$ $-2.263\,994\times10^{-16}T^4$ 2023 K and above: 7.8

[a] Reference 17.

[b] Reference 18.

[c] Reference 6.

[d] Reference 19.

[e] Reference 20.

[f] Due to the lack of relevant information, this value of the Poisson number is based on our control calculations described in the text and used for the rest of the study.

where α_{CIGS} is the absorption coefficient of CIGS, d_{ZnO} and d_{CIGS} are the thickness of the ZnO and CIGS layer, respectively. Due to the high absorption coefficient of Mo [approximately 5×10^5 cm^{-1} at 1064 nm (Ref. 22)], its optical absorption length is only about 20 nm. Hence, light absorption in the Mo was taken care of as a surface absorption as described in Eq. (3).

B. Heat diffusion

Heat diffusion within each layer was modeled by the three-dimensional transient heat-diffusion equation[15]

$$\rho C_p\frac{\partial T}{\partial t}=\nabla(k\nabla T)+\frac{\partial I(r,z,t)}{\partial z}, \tag{4}$$

where T is the absolute temperature while ρ, C_p, and k represent the density, specific-heat capacity, and heat conductivity of the layers, respectively. The second term on the right side of Eq. (4) refers to the heat source, i.e., the locally absorbed laser intensity. As explained in Sec. III, phase transitions were neglected.

When calculating the temperature field, the following boundary conditions were used:

$$T(r,\infty,t)|_{z=\infty}=T_0, \tag{5}$$

$$T(\infty,z,t)|_{r=\infty}=T_0, \tag{6}$$

$$\left.\frac{\partial T(r,z,t)}{\partial z}\right|_{z=0}=0, \tag{7}$$

$$\left.\frac{\partial T(r,z,t)}{\partial r}\right|_{r=0}=0. \tag{8}$$

The temperature distribution must also fulfill the following boundary conditions at each interface, namely, that (i) the temperature is continuous at every interface:

$$T_i|_{z=z_i}=T_{i+1}|_{z=z_i}, \tag{9}$$

and (ii) the heat flux for the two media in contact at each interface should be equal:

$$k_i\left.\frac{\partial T_i(r,z,t)}{\partial z}\right|_{z=z_i}=k_{i+1}\left.\frac{\partial T_{i+1}(r,z,t)}{\partial z}\right|_{z=z_i}. \tag{10}$$

In Eqs. (9) and (10), the subscript of T and k refers to the layer material, namely, ZnO (1), CIGS (2), Mo (3), and glass (4), while z_i $(i = 1, 2, 3)$ define the position of the ZnO/CIGS, CIGS/Mo, and Mo/glass interfaces along the z axis, respectively.

C. Thermal stress

Due to the rotational symmetry of our process, geometry cylindrical coordinates (r, ϕ, z, where z is the axis of symmetry) were used in our model calculations. The relevant equations describing the thermomechanical behavior of the samples are similar to those described in Refs. 23 and 24. The relationship between stress and strain is defined as

$$\underline{\sigma} = \underline{\underline{D}} \cdot \underline{\epsilon}_{\mathrm{elast}} = \underline{\underline{D}}(\underline{\epsilon} - \underline{\epsilon}_{\mathrm{th}}), \tag{11}$$

where $\underline{\sigma}$ is the stress vector, $\underline{\underline{D}}$ is the elasticity matrix, $\underline{\epsilon}_{\mathrm{elast}}$, $\underline{\epsilon}$, and $\underline{\epsilon}_{\mathrm{th}}$ is the elastic, total, and thermal strain vectors, respectively. The stress and strain vectors are given by the components of the stress and strain matrix, namely,

$$\underline{\sigma} = \begin{bmatrix} \sigma_{rr} \\ \sigma_{\phi\phi} \\ \sigma_{zz} \\ \sigma_{zr} \end{bmatrix}, \quad \underline{\epsilon}_{\mathrm{th}} = \frac{1}{3}\begin{bmatrix} \beta\,(T - T_0) \\ \beta\,(T - T_0) \\ \beta\,(T - T_0) \\ 0 \end{bmatrix},$$
$$\underline{\epsilon} = \begin{bmatrix} \epsilon_{rr} \\ \epsilon_{\phi\phi} \\ \epsilon_{zz} \\ \epsilon_{zr} \end{bmatrix} = \begin{bmatrix} \frac{\partial u_r}{\partial r} \\ \frac{u_r}{r} \\ \frac{\partial u_z}{\partial z} \\ \frac{1}{2}\left[\frac{\partial u_r}{\partial z} + \frac{\partial u_z}{\partial r}\right] \end{bmatrix}. \tag{12}$$

Due to the axial symmetry $\sigma_{\phi \mathrm{r}} = \sigma_{\mathrm{r}\phi} = \sigma_{\phi \mathrm{z}} = \sigma_{\mathrm{z}\phi} = 0$. In Eq. (12), T is the temperature that is originating from the temperature calculations and T_0 is the initial temperature of the sample (fixed at $T_0 = 293$ K for all of the calculations presented here).

If the material properties are isotropic, then the elasticity matrix $\underline{\underline{D}}$ can be expressed by the elastic modulus E and Poisson's ratio ν:

$$\underline{\underline{D}} = \frac{E}{(1+\nu)(1-2\nu)}\begin{bmatrix} 1-\nu & \nu & \nu & 0 \\ \nu & 1-\nu & \nu & 0 \\ \nu & \nu & 1-\nu & 0 \\ 0 & 0 & 0 & 1+2\nu \end{bmatrix}. \tag{13}$$

The principle of the virtual work was used to calculate the stress, which states that the virtual work made on a reference volume V by external forces is balanced by the virtual work of the internal stress and inertia:[25]

$$\int_V \delta\underline{\epsilon}^T \underline{\sigma}\, dv + \int_V \delta\underline{u}^T \rho \underline{\ddot{u}}\, dv = \int_S \delta\underline{u}_S^T \underline{F}_S ds, \tag{14}$$

where $\underline{\epsilon}$ is the total strain, $\underline{u}$ is the displacement, $\underline{u}_S$ is the displacement at the boundary, $\underline{F}_S$ is the applied force at the boundary, and δ and superscript T denote virtual changes and the transpose of vectors, respectively. The first term on the left side refers to the virtual work of elasticity within the reference volume, the second term describes the virtual work of the inertial force within the reference volume, and the term on the right side means the virtual work of the outer force acting on the surface of the reference volume.

The calculated stress field must fulfill a set of boundary conditions. Since there is no initial stress in the sample,

$$\underline{\sigma}|_{t=0} = 0. \tag{15}$$

Far from the irradiated area, the strain of the sample is always zero:

$$\underline{\epsilon}|_{x=y=z=0} = 0. \tag{16}$$

Since no outer force is acting on the surface, the stress-free surface boundary condition was used:

$$\sigma_{zz}|_{z=0} = 0, \quad \sigma_{rz}|_{z=0} = 0, \quad \sigma_{zr}|_{z=0} = 0. \tag{17}$$

IV. CALCULATION

Our simulations were performed using the structural mechanics module of COMSOL. The transient thermal stress model was solved, which is equivalent to the model described in Sec. III. In the calculations, cylindrical coordinates r,ϕ,z were used, where r is the radial, ϕ is the azimuthal component, and z is the axial coordinate along the symmetry axis. The dimensions of the calculation volume ($r_{\mathrm{max}} = 100\ \mu$m, $z_{\mathrm{max}} = 50\ \mu$m) were selected so that the set boundary conditions do not affect the obtained results. The calculation mesh was split into approximately 100 000 triangular areas using a nonuniform resolution. In all layers, the mesh was the finest, with sizes ranging from 0.1 to 0.3 μm, while in the glass substrate a coarser structure was used with sizes between 0.1 and 6 μm. Since outer force does not act on the thin-film structure, we used the (stress-) free surface boundary condition at the ZnO surface ($z = 0$), and fixed constraint was used as boundary conditions at the other boundaries of the modeled volume. The time resolution of the calculation (within the temporal window of 0–1 μs) was 0.1 ns since its further reduction had no effect on the results. In the simulations, the pulse energy and the size of the laser beam were varied in the same range that was used in our experiments.

A. Temperature field

The temperature profile along the symmetry axis ($r = 0$) can be seen in Fig. 3(a). Since the ZnO layer has no IR absorption, the majority of the incoming energy is absorbed in the CIGS layer. However, due to heat diffusion from the CIGS into the ZnO layer, the maximum temperature is shifted from the ZnO/CIGS interface into the deeper region of the CIGS layer. The maximum temperature, obtained within the sample during the entire heating cycle, is in the range of few 1000 K and occurs at 43 ns at the depth of approximately 0.4 μm in the CIGS layer. At this moment, the temperature is only about 330 K at the Mo/CIGS interface. After the end of the laser pulse, the temperature maximum shifts into the ZnO layer where the maximum temperature is in the order of 1000 K [cf. those curves in Fig. 3(a), which correspond to 200 and 300 ns]. The temperature rise of the Mo layer, however, remains in the order of few hundred Kelvin even after 300 ns and would approach 1000 K in the μs time domain if the CIGS and Mo layers will remain in physical and thermal contact in this

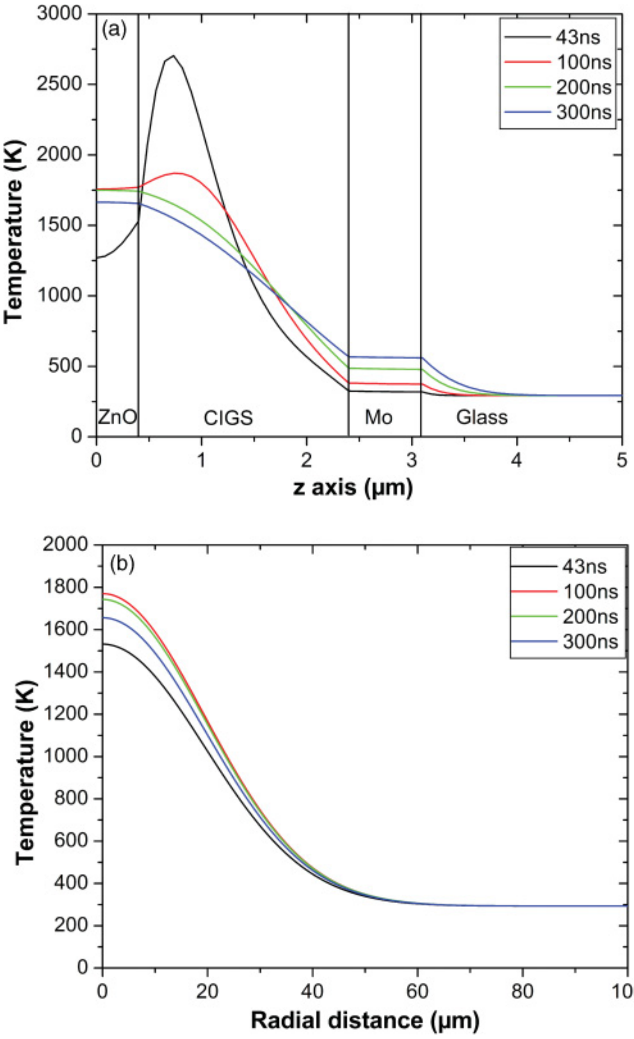

FIG. 3. (Color online) Calculated temperature distributions (at $F = 0.75$ J cm^{-2}, $w = 39$ μm) (a) along the axis of symmetry and (b) radially, at the ZnO/CIGS interface.

timescale. This proves that in our particular layer stack, only the CIGS and ZnO layers experience significant temperature rise, in the Mo layer the temperature increases only a few 100 K at most, and in the glass substrate the temperature rise is below 100 K.

In our calculations, the phase transitions (such as melting and evaporation) are neglected. As a consequence of this negligence, our calculation overestimates the temperatures in all cases where it is higher than the melting point of the CIGS layer, i.e., 1600 K (the CIGS has the lowest melting point and most part of the energy absorbed in it) because phase transitions require energy.

When comparing the radial temperature profile with the lateral intensity distribution of the laser beam, it can be asserted that the temperature profile, shown in Fig. 3(b), also follows a Gaussian distribution with exactly the same $1/e^2$ width as obtained for the incoming laser beam. This is so because heat diffusion in the radial direction is negligible in the 100-ns timescale, but of course the temperature profile will widen in the μs temporal domain. For checking the validity of our temperature calculation, the threshold fluence of the surface melting of CIGS was investigated. Experimentally, we obtained that the laser fluence corresponding to the onset of surface melting of the CIGS layer is within the 0.7–0.9 J cm^{-2} range. For these fluences, our temperature model predicts surface temperatures between 1650 and 1950 K. When comparing these to the melting point of CIGS (1600 K, cf. Table I), we obtain a 4%–25% overestimation of surface temperature. Since calculation-wise the 25% error includes the melting of the CIGS layer, below the melting point of CIGS the accuracy of our temperature calculations is less than 25%. All in all, the estimated temperature values have less than 25% error up to approximately 2000 K, and our calculations showed that the error can also be kept below 50% at temperatures as high as 3000 K.

In those cases when the calculation is performed above 0.9 J cm^{-2}, the maximum temperature may well exceed 3000 K. Since the temperature maximum lies inside the CIGS layer, the dominant evaporation mechanism is volume evaporation. Due to this effect, the hottest region removes the topmost part of the CIGS layer and hence the temperature calculation in the original layer structure would result in unrealistic temperature profiles.[15]

B. Stress field

Due to the lack of materials data, the Poisson number of CIGS was an unknown parameter in our calculations. In order to overcome this shortcoming, we performed test calculations in which we varied the Poisson number between 0.1 and 0.4. We found that in the 100-ns timescale, the Poisson number can only affect the value of the stress and has no significant effect on its spatial distribution. This means that the calculated stress values are unknown to a certain degree. As an example, when the Poisson number was varied from 0.4 to 0.1, the maximum stress value changed from −3.7 to −2.5 GPa. Since changing the Poisson number within this realistic regime causes less than an order-of-magnitude variation in the calculated stress values, we conclude that the calculated stress values are reliable to within an order of magnitude. All the data given in the present manuscript were obtained using a Poisson number of 0.4.

The radial and azimuthal components of the stress along the z axis are shown in Fig. 4(a) at 43 ns. It can be seen that the two stress profiles are practically identical. They have a maximum at 0.4 μm inside the CIGS layer, i.e., at the very same place where the temperature distribution peaks at the end of the laser pulse. The value of the peak stress is in the GPa range. As shown in Fig. 4(b), the lateral distributions of these stress components are almost the same in the radial direction as well. The temperature distribution was compared to the distribution of the radial and azimuthal components of the stress in both the radial and axial directions [cf. Figs. 4(c) and 4(d)]. In order to facilitate the comparison, the temperature and stress curves were normalized by dividing all data points of the curves by the maximum temperature and stress values that are reached in time and space (i.e., at $z = 0.4$ μm and $t = 43$ ns). The distribution of the temperature (solid curves) and the radial components of the stress field (dotted curves) are shown in Fig. 4(c) in the axial direction and in Fig. 4(d) in the radial direction at three different times. We found that the temperature and the stress distribution correlate well and

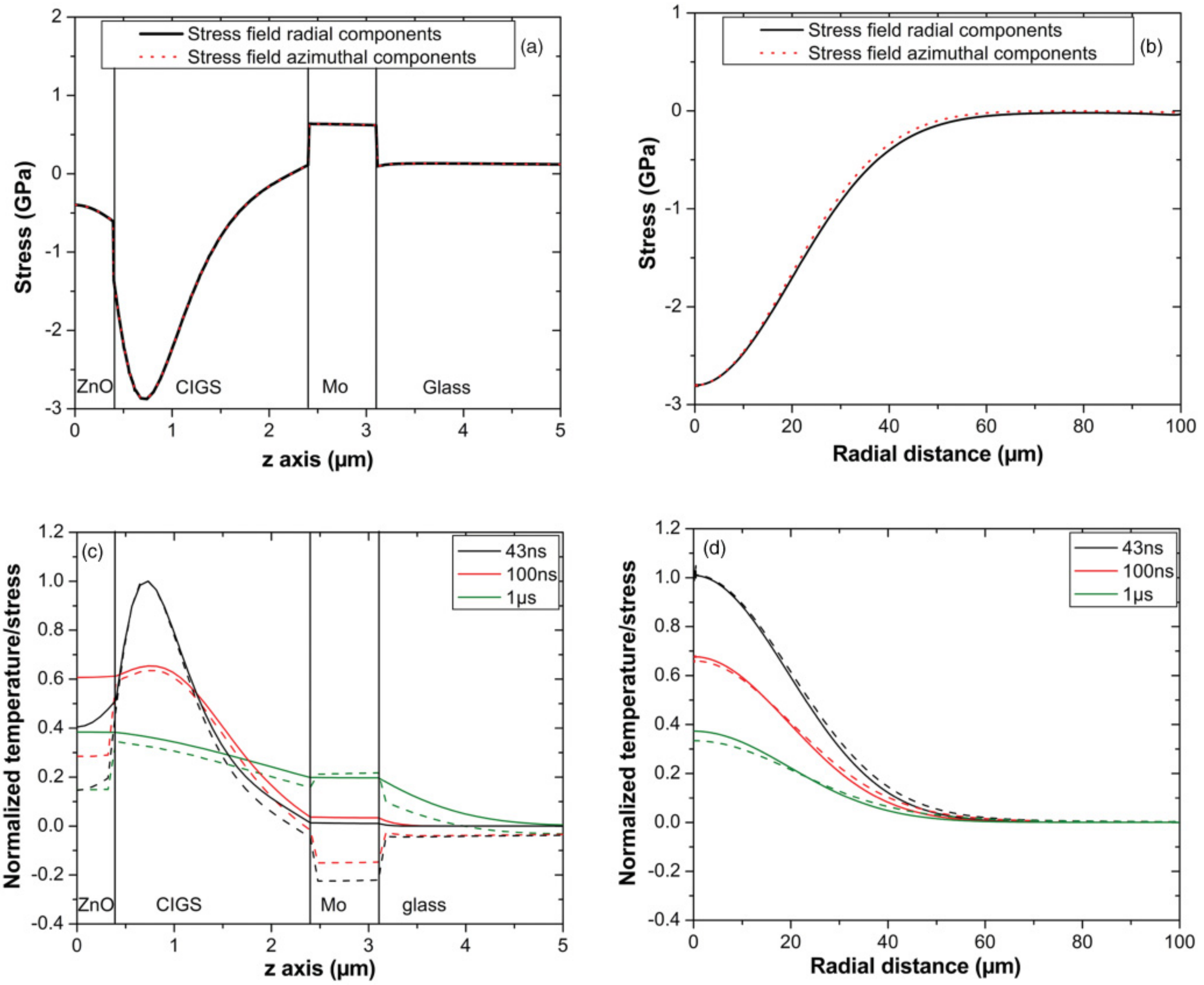

FIG. 4. (Color online) Calculated distribution (a) of the radial and azimuthal components of the stress along the axis of symmetry, (b) radial component of the stress in radial direction at 0.4 μm below the ZnO/CIGS interface at 43 ns. Normalized distribution of the temperature and radial components of the stress field in the (c) axial and (d) radial directions at 0.4 μm below the ZnO/CIGS interface. In graphs (c) and (d), continuous curves refer to temperature, while dotted ones indicate the stress. All data refer to $F = 0.75$ J cm^{-2} and $w = 39$ μm.

almost linearly within the CIGS layer, in all spatial directions and at every instance up to 1 μs. However, there is an inevitable difference between the stress and temperature distributions at the interfaces, where the stress values change abruptly, while the temperature follows a smooth transition. Due to the confirmed linear correlation of the stress and temperature inside the CIGS layer, it is plausible to assume that in the radial direction, the stress field also inherits the Gaussian distribution of the laser beam although the width of the stress distribution is slightly larger than 39 μm, i.e., the size of laser beam. The difference between the widths of the two distributions is less than 1 μm within the first 100 ns of the process.

We also studied the role of melting on the stress calculation. In the COMSOL model, we simulated the melting of the CIGS in such a way that the Young modulus of CIGS was set to zero when and where the local temperature reached the melting point, a condition equivalent to a stress-free boundary at the melt/solid interface. When comparing stress fields in the melt-free and molten cases, only a minor difference between the radial and azimuthal components of the stress field was obtained outside the molten region. This relievingly proves that during the highly nonequilibrium conditions realized by laser processing, melting has no effect on the radial and azimuthal components of the stress fields outside the melt pool.

V. RESULTS

A. Surface morphology

In our experiments, the pulse energy and spot size were varied. We found that the morphology of the patterned area can be put into one of the following three categories. At one extreme, exemplified in Fig. 5(a),*evaporation* is the dominant mechanism that determines crater morphology and leaves considerable amount of molten residue both inside and at the edge of the laser-processed area (this type will be referred to as E type). At the other extreme, shown in Fig. 5(b),

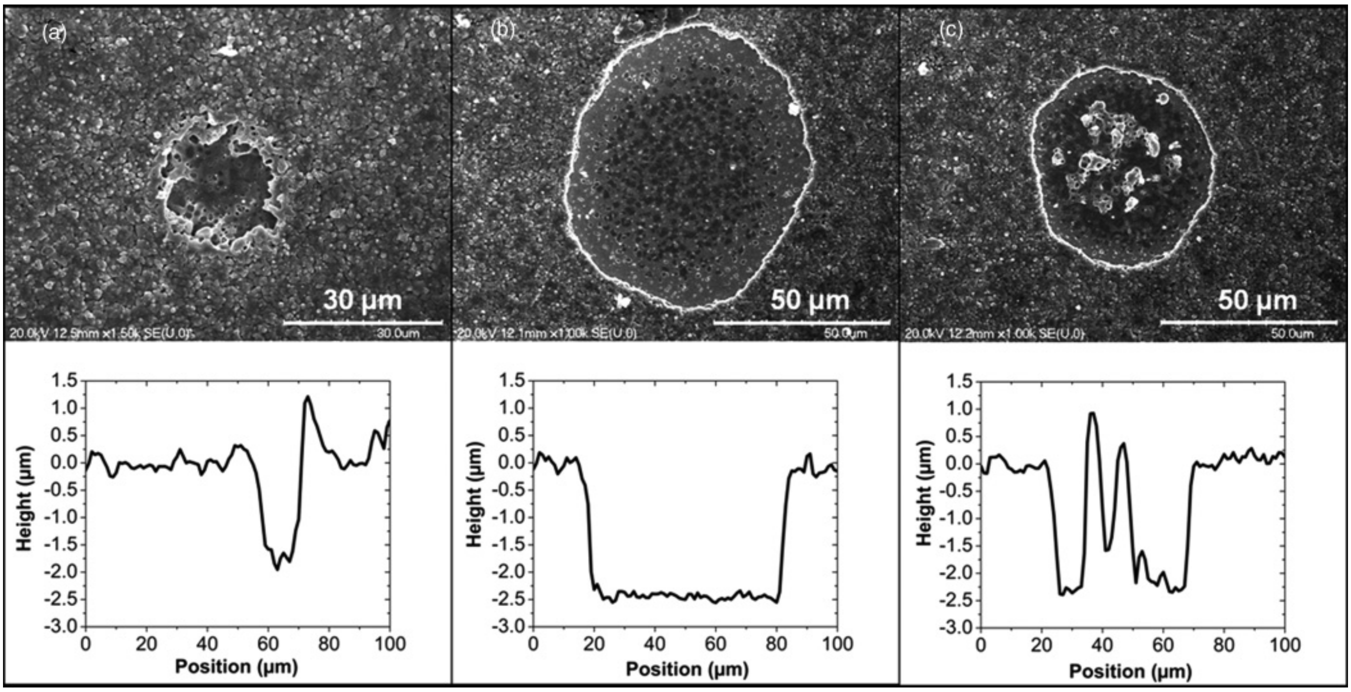

FIG. 5. Secondary electron micrograph of an ablation crater produced by the (a) evaporation ($F = 4.86$ J cm^{-2} and $w = 11.5$ μm), (b) thermally driven mechanical stress ($F = 0.842$ J cm^{-2} and $w = 44$ μm), and (c) competing evaporative and mechanical stress ($F = 2.41$ J cm^{-2} and $w = 26$ μm). Corresponding profilometric traces are also shown below each SEM image.

thermally driven *mechanical stress* is the dominant material removal mechanism which produces a rather different crater morphology (referred to as S type): there is a negligible amount of molten material in these craters, and the perimeter of the craters is not melted either. In-between these two ultimate types, a third, transitional category exists (referred to as M type due to its mixed nature), shown in Fig. 5(c), the craters of which exhibit the morphological characteristics of both the evaporative and the mechanical removal to some extent, and typically materializing in sharp crater edges but with considerable amount of molten residue inside it. Finally, at the lowest end of the fluence range, i.e., at fluences slightly below the threshold fluence characteristic to the S-type craters, the CIGS layer will not be removed, but laser treatment results in the bulging of the laser-irradiated zone (not shown in Fig. 5). While the sharp edges are typical to all craters in the S- and M-type morphological groups, the amount of molten residue inside the craters is far less in those identified as S type. Last, but not least, it is emphasized that the three morphological categories are introduced to describe the mechanism that dominantly determines crater morphology. Putting a particular crater in one of them, especially in the E and S types, does not mean that the corresponding mechanism is solely responsible for the removal of the entire amount of the ablated material. In many cases, both of the two fundamental mechanisms (namely, evaporation and mechanical stress) are taking place both laterally and in depth, but with respect to crater morphology only one of them is dominant (e.g., closer to the ZnO/CIGS boundary melting may be principal, but at the CIGS/Mo interface it is the stress that governs the material removal process and hence the latter determines the crater morphology).

Since avoiding damage to the Mo layer is crucial to the quality of the scribe, careful investigation of the SEM micrographs was executed in this respect. Our results proved that the Mo layer remains undamaged at the bottom of the craters within the M- and S-type morphological categories.

In order to estimate the amount of residue inside the ablated craters and the debris around them, the topography of the laser-patterned area was mapped by profilometry. Typical line traces for each type of craters are shown under each secondary electron micrograph of Fig. 5. In the case of E-type morphology, the average crater depth is approximately one micron [Fig. 5(a)]. When comparing crater depths with the total thickness of the ZnO and CIGS layers, that is, 2.5 μm, it can be concluded that significant amount of residue remains in these craters. Moreover, the amount of debris at the perimeter of the crater is also high: its typical height is in the μm range. As opposed to this, practically all the CIGS and ZnO are removed from those craters exhibiting S-type morphology [Fig. 5(b)], as evidenced by its typical depth of about 2.5 μm. The roughness of the crater bottom is typically around or less than 100 nm (proving that the molten residue in the center of the S-type craters forms less than 5% of the entire thickness of the ZnO and CIGS layers only) and there is no debris at the perimeter of these craters. Figure 5(c) shows the case when evaporative and mechanical (ablation) mechanisms compete in determining the crater morphology. The perimeter of the crater exhibits the morphology characteristic to mechanical ablation (brittle fractured edges and no debris), while in the center of the crater, there is considerable amount of residue that is similar to that observed in E-type craters. These molten remnants can even reach 2–3 μm in height.

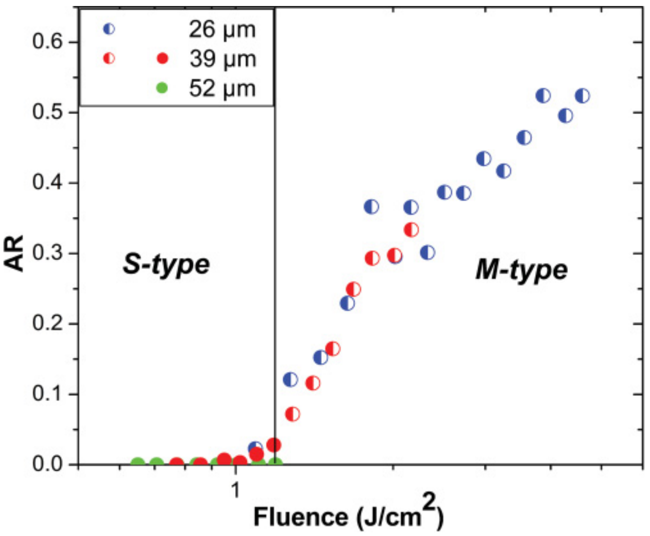

FIG. 6. (Color online) Area ratio *AR* of the molten residue covered inner area to the total area of the crater as a function of laser fluence used for creating them. Different colors depict craters made with different beam sizes. Closed and semiclosed symbols identify *S*- and *M*-type craters, respectively.

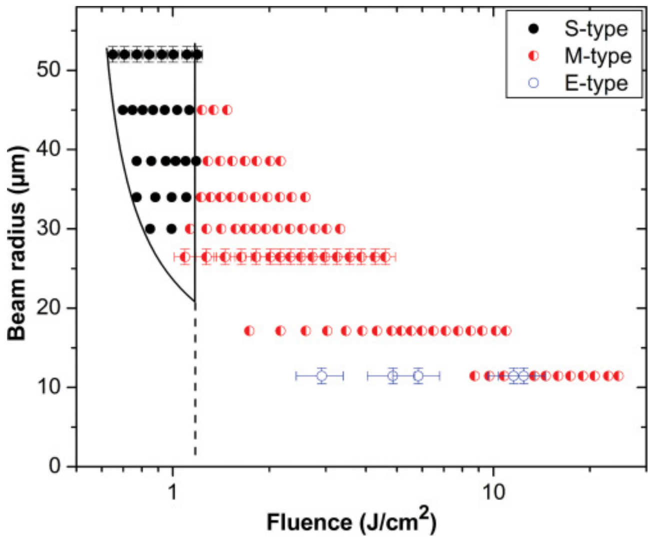

FIG. 7. (Color online) Spread of crater morphology type on the semilogarithmic beam radius vs fluence plane. Ablation was made in a glass/Mo/CIGS/ZnO:Al layer structure by a Nd:YAG laser ($\lambda = 1064$ nm, $\tau = 25$ ns). The typical error of the laser fluence and beam radii is indicated at several selected points.

By complementing the results of SEM with profilometry, the area where molten residue is significant can easily be differentiated. In order to determine the threshold fluence where morphology changes from *M* type to *S* type, the area of the molten region was normalized to the total area of the crater. In the actual procedure, both the total area of the crater and the melted region inside it were fitted by ellipses on each SEM image and the ratio of these two areas resulted in the area ratio *AR*, which is shown as a function of laser fluence in Fig. 6 at 26, 39, and 52 μm beam radii. We note that (i) the ablated areas are slightly elliptic in shape (i.e., the size of the crater along the scanning direction is about 6% larger than in the perpendicular direction) due to the fact that the sample is tilted with respect to the laser beam by 17.5° (cf. Fig. 1), and (ii) the SEM micrographs used for these evaluations were taken perpendicularly to the surface of the samples. It is obvious that in the normalized representation of Fig. 6, data referring to different beam sizes form a common trend. The most significant feature of this trend is the appearance of a threshold at about 1.1 J cm^{-2}.

Figure 7 shows how the three morphology types scatter on the fluence versus beam radius plane in a semilogarithmic representation. Please note that on the vertical axis of Fig. 7, the radius of the laser beam impinging on the surface of the sample is given, which is related but not identical to the radius of the crater created by the laser-material interaction. The radius of the laser beam was determined on Mo samples, as described in Sec. II. At selected data points, the estimated errors are also given in Fig. 7. The relative error is the largest at the smallest beam radius. Since the accuracy of the beam radius values is in the μm range, the maximum error of the fluence values was estimated to be about 20%–30% and below 5% at the smallest ($\approx$10 μm) and at the largest ($\approx$50 μm) laser beam radius, respectively. Figure 7 clearly demonstrates that the beam radius versus fluence representation is appropriate for separating the *S*-type morphological domain from the other two morphological types. Moreover, *S*-type morphology occurs in a distinct parameter domain, which will be referred to as clean mechanical ablation window, while the other two morphological domains overlap with each other. On the high-fluence side, this clean mechanical ablation window is bound by the 1.1-J cm^{-2} boundary (cf. Fig. 6) at all beam diameters. However, on the low-fluence side, the borderline between the bulged surface (bumped areas without CIGS removal) and the *S*-type craters is curved and the threshold fluence gradually shifts to smaller values as the beam diameter is increased.

B. EDS analysis

In the previous section, it was shown that craters with *S*-type morphology have excellent morphological characteristics, namely, only a small amount of residue was identified inside, but not close to the edge of the crater. EDS analysis was performed on numerous craters and elemental line scans typical to those of *S*-type morphology can be seen in Fig. 8(a). In the laser-processed zone, the x-ray signal of Cu, In, Ga, and Zn drops near to zero, accompanied by a significant increase in the Mo signal. These trends clearly, although only qualitatively, confirm that the majority of the CIGS and the ZnO:Al layers were removed when the laser-matter interaction results in an *S*-type crater. EDS analysis also indicates that from the elements of the active layer, only the Se signal remains non-negligible, identifying Se as the major component of the residue at the bottom of the *S*-type craters.

Figure 8(b) shows typical line scans obtained on a crater of *M*-type morphology. The Mo signal is very high at the perimeter of the crater and drops to approximately half of this value in the center region indicating considerable residues in this area. In the center region, mainly Se and In signals are

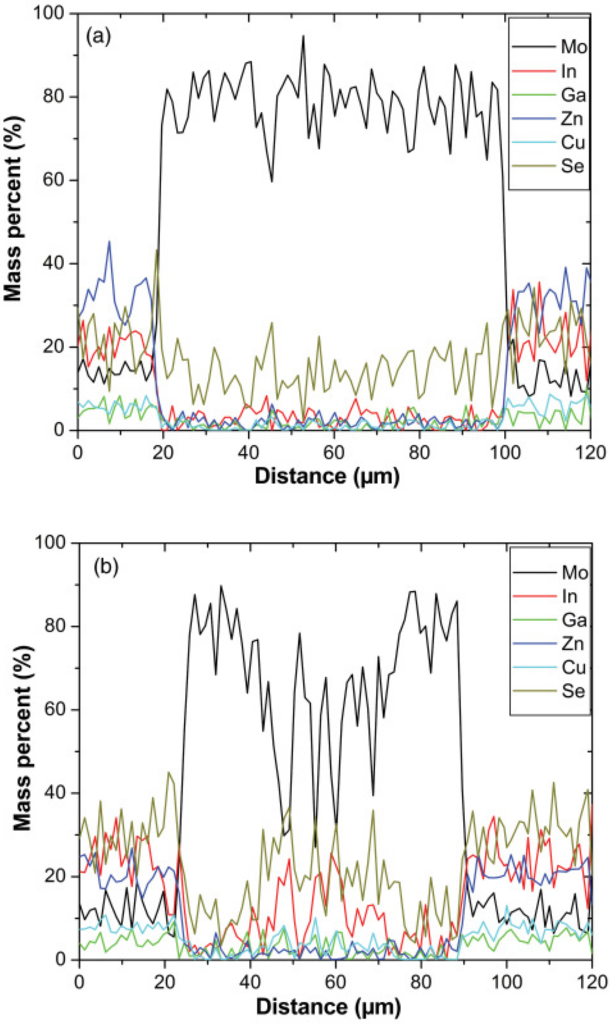

FIG. 8. (Color online) EDS line scans of six elements in two craters having (a) S-type ($F = 0.7\ \mathrm{J\ cm^{-2}}$) and (b) M-type morphology ($F = 1.50\ \mathrm{J\ cm^{-2}}$). All data were acquired at an accelerating voltage of 20 kV.

significant, and the signal of the other elements of the CIGS are near to zero.

The EDS analysis concludes that the small amounts of remnants in the craters having S-type morphology are made of Se. However, In and Se remain in the central region of craters of M-type morphology and in a much larger amount than in the S-type craters.

VI. DISCUSSION

As described briefly in Sec. I, two mechanisms can be responsible for mechanical removal of the CIGS layer, namely, vapor pillow formation at the Mo/CIGS interface and thermomechanical stress. Our morphological investigations proved that material remains in all crater types, i.e., minor, molten material can even be seen in the central regions of craters with S-type morphology [see Fig. 5(b)]. The molten nature of these residues indicates that the temperature at the CIGS/Mo interface is high enough to melt the interfacial region of the CIGS layer close to the Mo interface. Furthermore, from the morphological results, we can not exclude *a priori* that the temperature at the interface may even get high enough to eventually evaporate the interfacial layer, and hence to form a vapor pillow. In our case, the absorption coefficient of the CIGS layer was measured to be $2 \times 10^4\ \mathrm{cm^{-1}}$, meaning that most of the laser pulse's energy remains in the CIGS layer since, after passing its 2.0-μm thickness, only a few percent of the incident energy reaches the CIGS/Mo interface. Hence, heating of the CIGS/Mo interface occurs mostly by heat diffusion from the overlying hotter CIGS regions. Our temperature calculations show that a few-hundred-nanometer-thick CIGS region above the interface typically exhibits a 200–300 K temperature rise at the end of the laser pulse, and the maximum temperature rise is approximately 1000–1200 K in the μs time domain (cf. Fig. 3 in Sec. IV A).

If we assume that the chemical composition of the materials at the CIGS/Mo interface is CIGS and Mo, respectively, the interfacial temperature, calculated in our model, remains below 1200 K during the entire process, and can not explain the existence of molten remnants in the bottom of the crater since the melting point of both layers is considerably higher than the calculated temperature, i.e., $T_{\mathrm{mp,CIGS}} = 1600$ K, and $T_{\mathrm{mp,Mo}} = 2896$ K (cf. Table I). One possible explanation of this, and the existence of the Se(-rich) remnants we observed in the S-type craters [cf. Fig. 8(a)], is the presence of an interfacial layer between the CIGS and Mo layers, such as a $\mathrm{MoSe_2}$ or segregated Se layer, which has a considerably lower melting point than Mo or CIGS. $\mathrm{MoSe_2}$ reportedly forms during the deposition of the active layer with typical thicknesses of 10 to 100 nm, depending on the deposition procedure implemented, namely, whether the atmosphere is poor or rich in copper during the growth of the CIGS layer.[26] Since the relevant properties of $\mathrm{MoSe_2}$ are very much uncertain, in the following we will assume that the thermophysical properties of this low melting point interfacial layer can be estimated with that of elemental Se, namely, it exhibits a melting and boiling point of 494 and 958 K, respectively.

In order to obtain direct verification on whether the vapor pillow consisting of Se causes the mechanical ablation, we performed control experiments and irradiated the solar cell structure from the backside, i.e., through the glass substrate. Microscopic investigation of the irradiated areas processed in this backside geometry proved that selective removal of the CIGS layer from the Mo underlayer can not be achieved, and there was no sign of delamination at the CIGS/Mo interface, either. From the point of view of the temperature at the CIGS/Mo interface, there are two major differences between the two geometries: (1) The total reflectivity loss in the backside geometry is almost five times higher than in the normal geometry ($R_{\mathrm{air/ZnO/CIGS}} = 11\%$ and $R_{\mathrm{air/glass/Mo}} = 51\%$). (2) The Mo layer is a far better heat conductor than CIGS and hence the in-depth temperature profile that evolves in it in the backside geometry is almost flat, i.e., it is dissimilar to the significant temperature drop observed in the normal geometry [Fig. 3(a)]. When performing model calculations in the backside geometry, we accounted for both of these differences and obtained temperatures in excess of 3000 K at the Mo/CIGS interface by the end of the laser pulse. Although we changed the irradiation parameters in the same ranges, just like in the experiments, the maximum temperature is considerably larger than that obtained in the normal geometry. If a vapor pillow is formed, the larger interface temperatures should lead to larger pressures and more efficient layer removal. This prediction is in clear contradiction with our experimental observations, namely, the lack of delamination and selective layer removal in the backside experiments. Hence, we conclude that in our case vapor pillow formation at the CIGS/Mo interface is not the responsible mechanism of the mechanical ablation process.

Therefore, we propose the following stress-assisted ablation mechanism, which is largely governed by the stress field developing in the solid CIGS layer due to inhomogeneous laser heating. In our case, three phenomena play a crucial role in the mechanical ablation of the active layer, namely, (i) the separation of the CIGS and Mo layers, which will be referred to as *delamination*in the present context, (ii) *buckling*, which is the thermomechanical deformation of the CIGS and ZnO:Al layers that results in the bulging or bending out of these layers, and (iii) *fracture*, which is a mechanical failure process ultimately cracking the bulged layers at the perimeter of the craters. These three processes are interrelated. Delamination will make the CIGS layer practically freestanding in a circular area and facilitate the bending of the active layer away from the underlying Mo layer via the buckling process. Since buckling is confined, i.e., the CIGS layer deforms in a colder surrounding where the CIGS/Mo interface is intact (i.e., the layers are fixed to one another), it causes the development of a radial tensile stress at the perimeter of the strained region, which will lead to mechanical failure.

When laser irradiation commences, it initiates a temperature rise in the active layer of the solar cell which absorbs most of its radiation. Since the active layer is chemically inhomogeneous in depth (a shallow, low melting point layer is covered with a thick, high melting point CIGS), the upper and lower parts of the active layer behave differently. In the upper, solid part, a stress field is building up, while the lower, interfacial region gets melted at fairly low local temperatures. These processes are the fastest and strongest in the central part of the irradiated area (due to the lateral Gaussian intensity distribution of the illuminating laser pulse). As the temperature increases, a compressive stress is building up in the upper, solid CIGS layer, which will cause a moment to develop and will drive the buckling process. Our stress calculations proved that this compressive stress field in the solid CIGS film is the strongest at about 100 ns after the laser pulse. Therefore, we suppose that the separation of the layers will commence after about a few 100 ns and will first take place in the center of the laser-irradiated area. It will be here where the strained CIGS layer will first break apart from the underlying Mo one, most likely via tearing the molten interfacial layer apart. Then, the delamination front proceeds radially outwards. As the radius of delamination front grows, the interface gets colder and eventually delamination must separate a nonmolten interface. As compared to the separation of a molten layer, delamination of the solid active layer from the Mo layer proceeds via crack propagation and requires considerably more energy. Hence, the delamination process will cease shortly after the delamination front reaches the edge of the molten interfacial region and thus this solid phase process will define the very size of the circular area in which the active layer became freestanding. {The difference between the molten and solid phase delamination also materializes in the morphology of the remnants at the Mo surface, which is clearly different in the central and peripheral areas of the craters [cf. Fig. 5(b)]. Dark and light contrast on the secondary electron micrographs refer to molten and solid-phase delamination, respectively.} Then, the buckling of the CIGS layer may proceed further and increases the stress field within the CIGS layer. Ultimately, the radial tensile stress developing at the CIGS/Mo interface exceeds the fracture strength of the CIGS layer and the CIGS/ZnO:Al layers fail along the perimeter of the delaminated zone.[27]

The fact that we never observed a crater morphology where the CIGS layer was sticking out from the Mo one outside but in the vicinity of an S- and M-type crater suggests that the final size of the crater was determined by the delamination process. In the following, using the fundamentals of fracture physics we will show why and how delamination describes the experimental trends we observed. The key aspect lies in the Griffith's criterion, which describes the relation between the crack length a and the stress $\sigma_{\min}$ necessary to make it propagate:

$$\sigma_{\min}\sqrt{a} = K_C, \tag{18}$$

where K_C is a material constant. The very same relationship applies to cracks propagating along an interface[27,28] (e.g., the CIGS/Mo one) if a is identified as the radius of the delaminated area and K_C describes the adhesion of CIGS to the Mo layer. Although, in our case the separation of CIGS from Mo starts in a molten interfacial layer, the delamination front propagates beyond the central, melted region and it is here where crack propagation must fulfill the Griffith's criterion. Consequently, the Griffith's criterion will be responsible for defining the final size of the ablated crater.

Although we did not model the delamination process itself, as described above, we simulated the behavior of an inhomogeneously heated ZnO:Al/CIGS layer structure when it is detached from the Mo layer in a circular area. Our calculations verified that the CIGS and ZnO:Al layers will buckle in all cases. As it is shown in Ref. 29, the compressive radial stress, also present in our CIGS film, causes the moment that will bend out the freestanding circular thin film. Hence, in those cases when the ZnO:Al/CIGS layers are fixed to the Mo layer, there must also be a moment acting on these layers that try to move apart the ZnO:Al/CIGS layer stack from the Mo one. Moreover, since the radial compressive stress exhibits a Gaussian distribution in the CIGS layer [cf. Fig. 4(d)], we assumed that the stress field driving the crack propagation along the CIGS/Mo interface [i.e., $\sigma_{\min}$ in Eq. (18)] has a Gaussian lateral distribution, as well. Finally, both stress distributions inherit the $1/e^2$ width of the laser pulse, as it was proved in Sec. IV B. Under these conditions, the Griffith's criterion can be written as

$$c \cdot F \cdot e^{-\frac{2r^2}{w^2}} \sqrt{r} = K_C, \tag{19}$$

where r is the radius of the crater [and also equal to a, as explained after Eq. (18)], w is the radius of the laser beam on the sample surface and F is the peak laser fluence, as defined by Eq. (2b), and c is the scaling factor describing the relationship between $\sigma_{\min}$ and the intensity distribution of the laser. When solving this nonlinear equation for r at

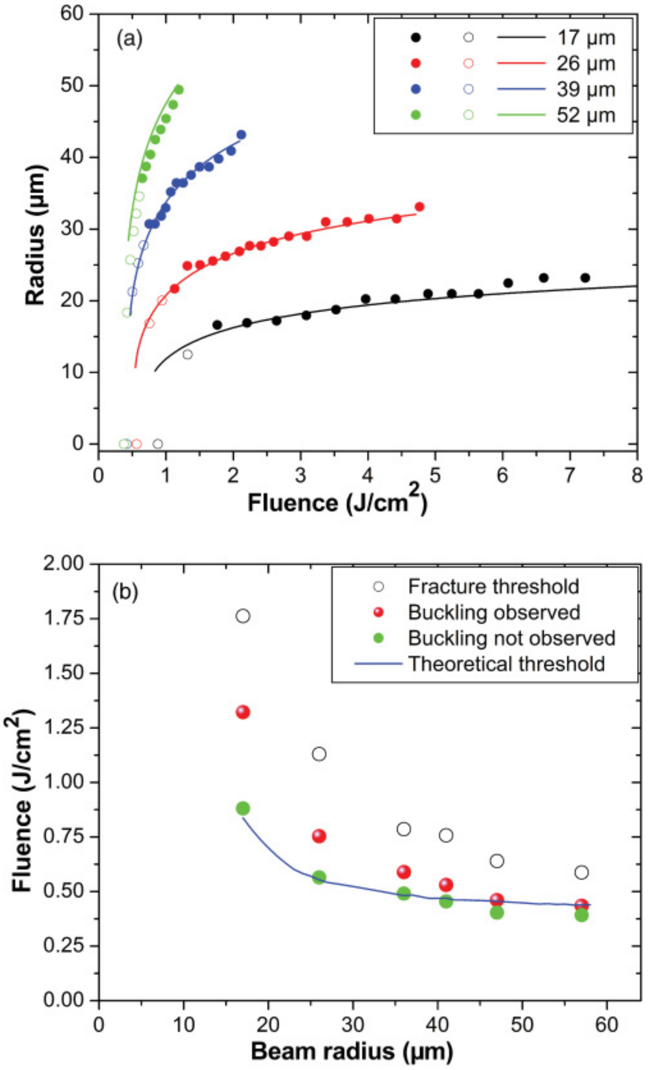

FIG. 9. (Color online) (a) Calculated radii fitted to the measured data (closed symbols: crater radius; open symbols: radii of buckled regions) and (b) the fluence threshold where fracture and delamination are observed at different beam radii.

different F and w values, we obtained the curves plotted in Fig. 9(a), which describe how the radius of the delaminated area is affected by the laser fluence and beam size. Since the curves, displaying the behavior of the delaminated area, fit very well to the tendencies of solid symbols, representing the crater sizes as a function of the experimental parameters, we conclude that the sizes of the craters are defined by the delamination process. It should be noted that the value of K_C is an unknown parameter, but we expect it to be constant for all of our experiments since it describes the adhesion of CIGS to Mo in our solar cell structure. And this is exactly what we got since all calculated curves plotted in Fig. 9(a) were obtained with a common K_C/c value, namely, 12.987 J m^{-2} m$^{1/2}$, and they convincingly fit all crater sizes at every pulse energy and beam diameter used.

When the laser fluence and beam diameter are outside but close to the lower end of the clear mechanical ablation window (i.e., to the left of the clear mechanical ablation window in Fig. 7), the removal of the CIGS film does not take place, but the laser-illuminated areas are bulged and in a few cases partially fractured areas, such as the one shown in Fig. 10, can also be found. Electron microscopic investigation of such partially fractured areas proves that (i) bulging is formed by the buckling of the layer, and the contribution of thermal expansion (normal to the surface) to bulging is negligible since there is no measurable difference in the thickness of the fractured CIGS layer in the central hotter and the outer colder regions (cf. Fig. 10), and (ii) wherever the surface of the laser-irradiated area is buckled, the process is always accompanied by the delamination of the CIGS layer and the size of the buckled and delaminated areas are exactly the same (cf. that fracture of the CIGS and ZnO:Al layers occurs at the very edge of the delaminated area in Fig. 10). The latter means that bulging of the sample surface can be considered as an evidence of delamination at the CIGS/Mo interface, and in all those cases when the removal of the CIGS and ZnO:Al layers does not take place but bulging of the surface is observed, the diameter of the buckled region is a suitable estimate to the size of the delaminated area.

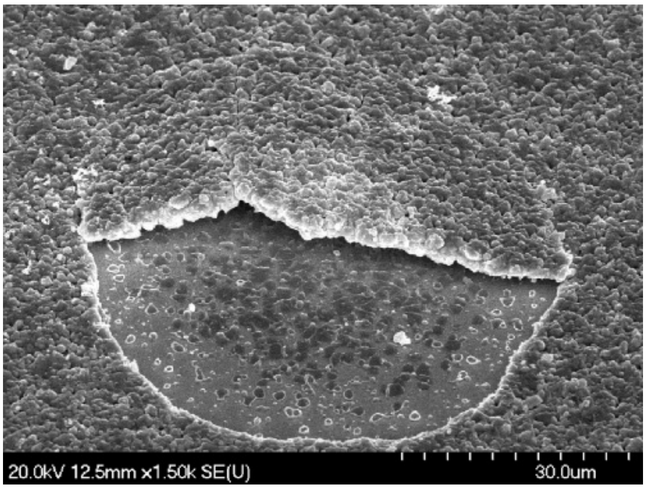

FIG. 10. Secondary electron micrograph of a sample surface, which became bulged and partially fractured due to laser irradiation ($F = 0.66$ J cm^{-2}, $w = 44$ μm).

Therefore, we scanned the area around the buckled zones by profilometry and plotted the diameter of the buckled area with open symbols in Fig. 9(a) along with the diameter of the craters, shown with closed symbols. The fact that open and closed symbols are part of the very same diameter versus fluence curves proves that the onset of fracture has no effect on these curves. Consequently, fracture must be independent of the delamination process, which is easily satisfied if we assume that delamination is fully accomplished before fracture starts to proceed, which is important information on the relative progress of these two governing processes.

We also attempted to estimate the threshold fluence of delamination $F_{\text{th,delam}}$. Experimentally, we could only set an upper and lower limit to this threshold fluence due to the discrete nature of our beam size and laser fluence data set. At every beam diameter, the upper limit is set by the last fluence value where surface buckle was observed, while the lower limit is defined by the next consecutive fluence value where buckle was not observed. In Fig. 9(b), these maxima and minima are plotted as a function of beam radius. The threshold fluence of delamination must run between these two values. We also calculated this fluence threshold and plotted its value as a solid curve. Figure 9(b) evidences good agreement between the calculated curve and the experimentally determined fluence domain.

Finally, in Fig. 9(b), we also plotted the laser fluences corresponding to the onset of layer fracture $F_{\mathrm{th,fract}}$ and observed that fracture is initiated at decreasing laser fluence if we increase the laser beam radius. Although not all the details are understood yet, the qualitative explanation of this tendency is as follows. The fracture of the CIGS and ZnO:Al layers is preceded by their buckling. The magnitude of the tensile stress at the perimeter of the crater depends on the extent of buckling, which, aside from the materials' properties, is most influentially set by the geometry of the bulged films. As a first approximation, this geometrical factor scales with a/h, where a is the radius of the delaminated disk ($a = r$) and h is the thickness of the layers. The larger the a/h, the easier the buckling is, which materializes in a smaller threshold fluence of fracture $F_{\mathrm{th,fract}}$.

Our experiments were performed on an entire solar cell layer structure where the topmost ZnO:Al layer was removed. Since experiments performed with or without the window ZnO:Al layer showed very similar results, it is reasonable to assume that the 400-nm-thick ZnO:Al layer does not change significantly the thermomechanical behavior of the layer structure and has negligible influence on the mechanical ablation process. As a corollary, we may also conclude that the principal driving force of mechanical ablation is the mechanical stress developing within the outbending CIGS layer. From this we can also conclude that the process that governs the size of the ablation craters should be one that either solely acts within the CIGS layer or at the CIGS/Mo interface, which is in line with our previous conclusion that it is the delamination process that sets the size of the ablation craters.

It is clear that the left-hand-side boundary of the clear mechanical ablation window (cf. Fig. 7) is set and hence governed by the above-described stress-related phenomena developing in the solar layer structure due to laser irradiation. However, the upper fluence boundary of the ablation window, which was measured to be constant at 1.1 J cm^{-2}, is clearly determined by a thermal phenomenon, most likely by the melting of the CIGS layer. These two boundaries then embrace the practically most useful region of the fluence-beam size parameter space where clear mechanical ablation can be performed and results in craters exhibiting S-type morphology. Although from the practical viewpoint laser patterning is more appealing if performed around the left boundary, in the following we will briefly describe the right-hand side, thermal limit, as well. Due to intense heating, the melting front penetrates up to a certain depth. The final outcome of the material removal process, namely, whether an S- or M-type crater is formed, largely depends on how the depth of this melt pool compares to the total thickness of the CIGS layer. When the melt pool is shallow enough, the mechanical stability of the underlying solid CIGS layer is high and hence strong enough to carry away the molten material above it, which alternately results in an S-type crater morphology. However, when the melted region gets deeper (i.e., the melting front moves closer to the CIGS/Mo interface), the solid CIGS layer underneath it (if any) can not take it off and considerable amount of molten material remains in the crater, resulting in an M-type morphology after resolidification. Due to the Gaussian intensity distribution of the initiating laser pulse, more resolidified remnants appear in the centermost part of the laser-irradiated area.

From the point of view of module patterning, the S-type morphology has very appealing properties. At low beam radius (e.g., at 30 μm), the practical fluence domain in which S-type morphology can be formed is very narrow. However, with increasing beam radius, the fluence domain where the mechanism is stable becomes wider as verified by the closed symbols in Fig. 7. The width of the S-type domain in laser fluence, when the beam radius is above 30 μm, is wide enough to allow convenient implementation of the laser process via the identified, stress-assisted ablation mechanism.

VII. CONCLUSIONS

Extensive investigations on nanosecond laser ablation of CIGS-based solar cell structure, both experimentally and theoretically, were performed in which the energy and size of the laser beam were systematically varied in a wide range. We demonstrated that laser pulses of nanosecond duration originating from an industrial friendly Nd:YAG laser are capable to remove the CIGS (and ZnO:Al) layer(s) and result in an excellent crater morphology, which is dominantly formed by mechanical effects.

It was proved that evaporation at the Mo/CIGS interface can not be the process that drives the mechanical ablation. Instead, we proposed a model in which material removal is governed by the thermomechanical stress developing in the CIGS layer due to intense laser heating. In this model, three phenomena play a crucial role in the mechanical ablation of the active layer, namely, *delamination*, *buckling*, and *fracture*. Delamination ultimately determines the size of the craters, which proceed independently of fracture. The delamination and the buckling process are driven by the compressive stress that arises in the CIGS layer. Finally, the fracture of the CIGS layer occurs since buckling produces a tensile stress at the perimeter of the craters.

To verify our mechanical ablation model, numerical calculations were performed using the COMSOL software where the laser-induced temperature and stress field in the solar cell structure were modeled. Our calculation predicts such a stress distribution that was capable to describe the delamination where Griffith's criterion was used to estimate the delaminated area, and all crater sizes can be fitted using a well-chosen K_C value that describes the adhesion of the CIGS and the Mo layer.

ACKNOWLEDGMENTS

The financial support of the OTKA TS049872 and NKFP 3/025/2001 grants is kindly acknowledged. The generous assistance of J. Kopniczky in performing electron microscopic and profilometric measurements is greatly appreciated.

[*] buzas@brc.hu

[1] H. Yu, D. D. Dlott, and F. R. Kearney, J. Imaging Sci. Technol. **50**, 401 (2006).

[2] D. Karnakis, A. Kearsley, and M. Knowles, J. Laser Micro/Nanoeng. **4**, 218 (2009).

[3] P. Jackson, D. Hariskos, E. Lotter, S. Paetel, R. Wuerz, R. Menner, W. Wischmann, and M. Powella, Prog. Photovolt: Res. Appl. **19**, 894 (2011).

[4] F. Kessler and D. Rudmann, Sol. Energy **77**, 685 (2004).

[5] F. Kessler, D. Herrmann, and M. Powalla, Thin Solid Films **480-481**, 491 (2005).

[6] A. D. Compaan, I. Matulionis, and S. Nakade, Opt. Laser Eng. **34**, 15 (2000).

[7] P. O. Westin, U. Zimmermann, M. Ruth, and M. Edoff, Sol. Energy Mater. Sol. Cells **95**, 1062 (2011).

[8] P. O. Westin, U. Zimmermann, and M. Edoff, Sol. Energy Mater. Sol. Cells **92**, 1230 (2008).

[9] J. Hermann, M. Benfarah, S. Bruneau, E. Axente, G. Coustillier, T. Itina, J.-F. Guillemoles, and P. Alloncle, J. Phys. D: Appl. Phys. **39**, 453 (2006).

[10] P. Gečys, G. Račiukaitis, E. Miltenis, A. Braun, and S. Ragnow, Phys. Procedia **12**, 141 (2011).

[11] G. Heise, M. Domke, J. Konrad, F. Pavic, M. Schmidt, H. Vogt, A. Heiss, J. Palm, and H. P. Huber, Phys. Procedia **12**, 149 (2011).

[12] D. Ruthe, K. Zimmer, and T. Höche, Appl. Surf. Sci. **247**, 447 (2005).

[13] M. Rekow, R. Murison, T. Panarello, C. Dunsky, C. Dinkel, S. Nikumb, J. Pern, and L. Mansfield, 25th European Photovoltaic Solar Energy Conference PVSEC/WCPEC-5 Valencia, Spain, 2010 (unpublished); R. Murison, C. Dunsky, M. Rekow, C. Dinkel, J. Pern, L. Mansfield, T. Panarello, and S. Nikumb, 35th IEEE Photovoltaic Specialists Conference, Honolulu, 2010 (unpublished).

[14] J. Bovatsek, A. Tamhankar, R. S. Patel, N. M. Bulgakova, and J. Bonse, Thin Solid Films **518**, 2897 (2010).

[15] D. Bäuerle, *Laser Processing and Chemistry* (Springer, Berlin, 2000).

[16] J. M. Liu, Opt. Lett. **7**, 196 (1982).

[17] S. Deriano, T. Rouxel, S. Malherbe, J. Rocherulle, G. Duisit, and G. Jezequel, J. Eur. Ceram. Soc. **24**, 2803 (2004); M. H. M. Zaid, K. A. Matori, L. C. Wah, H. A. A. Sidek, M. K. Halimah, Z. A. Wahab, and B. Z. Azmi, Int. J. Phys. Sci. **6**, 1404 (2011); A. Issa, D. Brabazon, and M. S. J. Hashmi, J. Mater. Process. Technol. **207**, 307 (2008).

[18] H. Shinno, M. Kitajima, and M. Okada, J. Nucl. Mater. **155–157**, 290 (1988); H. Hashizume and K. Miya, Fusion Eng. Des. **5**, 141 (1987).

[19] T. Tinoco, A. Polian, D. Gómez, and J. P. Itié, Phys. Status Solidi B **198**, 433 (1996).

[20] COMSOL database, COMSOL 4.0a, 2010.

[21] *CRC Handbook of Chemistry and Physics*, edited by David R. Lide (Taylor and Francis, Boca Raton, FL, 2006).

[22] D. W. Lynch and W. R. Hunter, in *Handbook of Optical Constants of Solids*, edited by E. D. Palik (Academic, San Diego, 1998).

[23] L. D. Landau and E. M. Lifshitz, *Theory of Elasticity* (Nauka, Moscow, 1986; Pergamon, Oxford, 1986).

[24] D. Albagli, Ph.D. thesis, Massachusetts Institute of Technology, Cambridge, 1994.

[25] M. E. Gurtin, E. Fried, and L. Anand, *The Mechanics and Thermodynamics of Continua* (Cambridge University Press, New York, 2009).

[26] T. Wada, N. Kohara, S. Nishiwaki, and T. Negami, Thin Solid Films **387**, 118 (2001).

[27] M. Reichling, A. Bodemann, and N. Kaiser, Thin Solid Films **320**, 264 (1998).

[28] M. Nagai, T. Ikeda, and N. Miyazaki, Eng. Fract. Mech. **74**, 2481 (2007).

[29] R. F. Barron and B. R. Barron, *Design for Thermal Stresses* (Wiley, Hoboken, New Jersey, 2011).